Appl Phys A (2011) 105:167–176
DOI 10.1007/s00339-011-6463-4

Applied Physics A
Materials Science & Processing

Nanosecond and femtosecond ablation of $La_{0.6}Ca_{0.4}CoO_3$: a comparison between plume dynamics and composition of the films

S. Canulescu · E. Papadopoulou · D. Anglos · T. Lippert · M.J. Montenegro · S. Georgiou · M. Döbeli · A. Wokaun

Received: 11 October 2010 / Accepted: 25 April 2011 / Published online: 27 May 2011

Abstract Thin films of $La_{0.6}Ca_{0.4}CoO_3$ were grown by pulsed laser ablation with nanosecond and femtosecond pulses. The films deposited with femtosecond pulses (248 nm, 500 fs pulse duration) exhibit a higher surface roughness and deficiency in the cobalt content compared to the films deposited with nanosecond pulses (248 nm, 20 ns pulse duration). The origin of these pronounced differences between the films grown by ns and fs ablation has been studied in detail by time-resolved optical emission spectroscopy and imaging. The plumes generated by nanosecond and femtosecond ablation were analyzed in vacuum and in a background pressure of 60 Pa of oxygen. The ns-induced plume in vacuum exhibits a spherical shape, while for femtosecond ablation the plume is more elongated along the expansion direction, but with similar velocities for ns and fs laser ablation. In the case of ablation in the background gas similar velocities of the plume species are observed for fs and ns laser ablation. The different film compositions are therefore not related to different kinetic energies and different distributions of various species in the plasma plume which has been identified as the origin of the deficiency of species for other materials.

S. Canulescu (✉)
Department of Photonics Engineering, Technical University of Denmark, 4000 Roskilde, Denmark
e-mail: stec@fotonik.dtu.dk

E. Papadopoulou · D. Anglos · S. Georgiou
Institute of Electronic Structure and Laser, Foundation for Research and Technology-Hellas, P.O. Box 1385, 71110 Heraklion, Greece

E. Papadopoulou
e-mail: eviep@iesl.forth.gr

S. Georgiou
e-mail: sgeorgiu@iesl.forth.gr

D. Anglos
e-mail: anglos@iesl.forth.gr

D. Anglos
Department of Chemistry, University of Crete, P.O. Box 2208, 710 03 Heraklion, Greece

T. Lippert (✉) · A. Wokaun
Department of General Energy Research, Paul Scherrer Institut, 5232 Villigen, Switzerland
e-mail: thomas.lippert@psi.ch

A. Wokaun
e-mail: alexander.wokaun@chem.ethz.ch

M.J. Montenegro
ALSTOM AG, Zentralstrasse 40, 5242 Birr, Switzerland
e-mail: macarena.montenegro@power.alstom.com

M. Döbeli
Laboratory of Ion Beam Physics, ETH Zurich, 8093 Zurich, Switzerland
e-mail: doebeli@phys.ethz.ch

1 Introduction

Femtosecond lasers of high intensities ($<10^{18}$ W/cm^2) are currently used to process transparent materials via multiphoton absorption, and can be applied for the fabrication of photonic crystals [1] or 3D structures by two-photon polymerization [2]. Laser ablation with fs pulses allows high-quality structuring with almost no heat affected zone [3]. Low power fs lasers have been also used to generate X-rays from liquid targets [4]. Furthermore, the interaction of ultrahigh intensity femtosecond pulses ($>10^{18}$ W/cm^2) with matter can act also as a source of high energy electrons [5], γ-ray pulses [6], ions [7], neutron beams [8], as well as

X-rays of unique properties. The emission of the fast particles and short wavelength radiation is expected to be ultrashort, while the source area is in the range of the area of the laser spot; at these ultrahigh intensities the emission becomes anisotropic and the generated hot electrons become relativistic [9]. These characteristics of a source of excellent brightness may be used in sub-picosecond time-resolved diffraction experiments, and imaging in ultrashort wavelength lithography [10].

Ultrashort pulses have been also used for producing high-quality materials by pulsed laser deposition (PLD). The general idea of using pulses of duration shorter than the electron–phonon coupling time in solids is to minimize the formation of droplets, which are often observed in ns ablation [11]. It was generally assumed that ultrashort pulses would be sufficient to preserve the stoichiometry of the target. Femtosecond pulses have been successfully used for the deposition of polymers [12], semiconductors, such as SiC and AlN [13], diamond like carbon (DLC) [14], and other hard coating materials, such as Al-Mg-B-Ti [15] and BC [16], but the data published until now are not showing that fs-PLD can be a general approach for depositing thin films.

We have grown $La_{0.6}Ca_{0.4}CoO_3$ thin films by ns ablation and have shown that it is possible to obtain films with low surface roughness, and that the film crystallinity can be controlled by varying the deposition temperature, substrate material and cooling conditions [17]. $La_{0.6}Ca_{0.4}CoO_3$ (LCCO) is used as bifunctional catalyst in metal–air batteries and is applied in rechargeable zinc/air batteries [18]. It was shown that the catalytic activity of the LCCO thin films depends to a large extent on their crystallinity [17]. However, high-quality epitaxial films produced by ns-PLD have oxygen deficiencies that compromise material crystallinity.

In this paper we study the laser-matter interaction in the femtosecond regime compared to the nanosecond regime for LCCO. The main aim is to study to which extent fs pulses can be applied for depositing complex oxides, and whether the stoichiometry of the target can be preserved, including the oxygen content.

2 Experimental

2.1 Material and methods

Ablation experiments were carried out in a vacuum chamber evacuated to a residual pressure of 10^{-4} Pa. The target was rotated during ablation to minimize crater formation. Ns-KrF ($\lambda = 248$ nm, $\tau = 20$ ns) and fs-KrF excimer lasers ($\lambda = 248$ nm, $\tau = 500$ ns) were used for deposition and spectroscopic investigations. The ns beam was focussed on the target on a spot area of 1.5 mm^2, which corresponds to a laser fluence of 5 $J\,cm^{-2}$. In the case of the fs experiments, the laser spot on the target was 0.5 mm^2, resulting in a laser fluence of 3 $J\,cm^{-2}$. The substrate to target distance was kept constant at 4 cm. The number of laser pulses was adjusted to obtain films with an average thickness of 150 nm.

Different pressures of oxygen background (60, 250, 400, and 600 Pa O_2) were used for optimizing the deposition conditions. The films were grown on MgO (100) substrates at a temperature of 650°C. The surface morphology of the films was investigated by Atomic Force Microscopy (AFM). The film composition was determined on the basis of Rutherford Backscattering (RBS) measurements performed with a 2 MeV ^{4}He beam and a silicon surface barrier detector at 165 degrees. The collected RBS data were simulated using the RUMP software.

Space- and time-resolved emission spectroscopy measurements of the plume were performed both in vacuum and at 60 Pa O_2 pressure. The spectra were collected by focussing the emission onto a quartz fibre (at 1:1 magnification configuration), through an appropriate observation port on the chamber. The exit of the fibre was coupled onto the entrance slit of a spectrograph (TRIAX-320, Jobin Yvon-Spex) equipped with three holographic diffraction gratings, 600, 1800 and 2400 lines/mm, providing spectral resolutions of 0.4, 0.15 and 0.1 nm, respectively. The emission was recorded by an intensified charged couple device (ICCD, DH520-18F, Andor technology) gated for an interval of 40 ns. Emission spectra were investigated in the range of 300–900 nm. The spatially resolved emission spectra were collected by translating the input of the fibre along the target surface normal, i.e. along the plume expansion. The spatial resolution was 0.5 mm. The temporal evolution was also studied for delay times in the range of 120 ns to 2120 ns. The minimum delay time, with respect to the laser pulse, was 120 ns and was imposed by the response of the electronics.

The plume imaging was monitored by decoupling the ICCD camera, working in time-gated detection mode, from the spectrograph and focussing the optical emission onto the 1024×256 diode array with a 1:1 magnification. Either the total emission was recorded, or just a fraction of the emission transmitted through band pass interference filters, which were chosen accordingly for each species. For the ns experiments, the gate width was 15 ns with 10 accumulations per image, while for fs experiments a gate width of 30 ns and up to 50 accumulations per image were used.

3 Results

3.1 Film composition, structure and morphology

Main goal of this study has been to investigate the influence of laser pulse duration on the structural, morphological, and

compositional properties of $La_{0.6}Ca_{0.4}CoO_3$ (LCCO) films grown by PLD. Experiments carried out at different oxygen background pressures, in the range of 60, 250, 400 and 600 Pa O_2, showed optimum deposition conditions to be at a background pressure of 60 Pa O_2 in both ns and fs PLD. The substrate temperature (T_s) and target to substrate distance $d_{T\text{-}S}$ were kept constant, at "typical" values used for ns deposition, i.e. $T_s = 650°C$ and $d_{T\text{-}S} = 4$ cm.

Concerning morphology, a direct comparison of surface profiles obtained by AFM shows clearly that the roughness of films grown by fs-PLD is significantly higher than that of the films grown by ns-PLD. Films deposited by fs ablation (Fig. 1a) exhibit large grains with an average particle size of 900 Å, and roughness on the order of 250 Å (RMS). The roughness of the ns-PLD grown films (Fig. 1b) is much lower (approximately 10 Å), while their surface morphology exhibits small conical structures regularly distributed on the film surface. This, according to Thornton's model, corresponds to a Zone I microstructure [19].

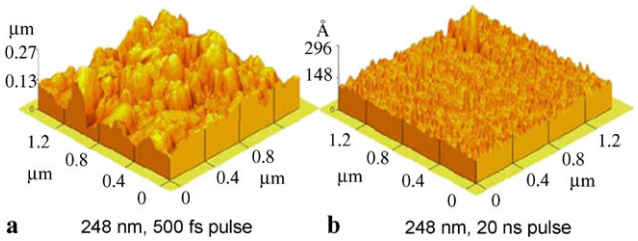

Fig. 1 A. AFM images of the $La_{0.4}Ca_{0.6}CoO_3$ thin films deposited on MgO(100) with femtosecond laser ($\lambda = 248$ nm, 500 fs), B. with nanosecond laser ($\lambda = 248$ nm, 20 ns)

Film crystallinity was studied by XRD, and relevant data are shown in Fig. 2. Films produced by nanosecond ablation show a preferential orientation in the (200) plane as well as a number of additional diffraction peaks corresponding to other oxide phases. Single oriented films are obtained when a fast cooling procedure is applied [17]. The femtosecond produced films do not show any peaks attributed to the LCCO crystalline perovskite phase, but other secondary phases, such as CoO_x and CaO_x, are present. However, we cannot exclude the presence of LCCO amorphous phase which cannot be detected by XRD.

The elemental composition of the films, as determined by RBS, reveals that as deposited films are oxygen deficient (see Table 1). Films grown by femtosecond ablation reveal as well a strong deficiency in the Co content with respect to the original target stoichiometry, i.e. $La_{0.6}Ca_{0.4}CoO_{3-\delta}$. It is noteworthy that the rough surface of the films prepared by fs ablation makes the measurement and simulation of the RBS spectra difficult, which results in relatively large uncertainties.

3.2 Optical emission spectroscopy

In an effort to better understand the influence of deposition parameters on film stoichiometry and morphology, time- and space-resolved emission spectroscopy and time-resolved plume-imaging experiments have been performed. More specifically, it has been investigated how plume properties, such as composition, expansion velocity, and angular distribution, in ns and fs ablation might influence the deposition stoichiometry.

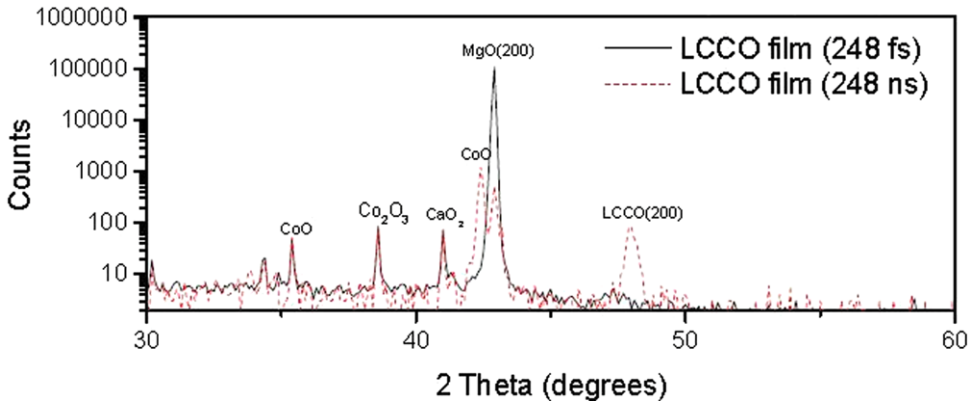

Fig. 2 XRD spectra of LCCO films deposited on MgO(100) using different pulse lengths

Table 1 Comparison between morphological, structural and composition properties of the LCCO films deposited on MgO(100) using different pulse lengths

	PLD (248 nm, 20 ns pulse)	PLD (248 nm, 500 fs pulse)
RBS	$La_{0.66\pm0.03}Ca_{0.34\pm0.01}Co_{0.97\pm0.02}O_{2.7\pm0.2}$	$La_{0.69\pm0.03}Ca_{0.31\pm0.01}Co_{0.69\pm0.03}O_{2.7\pm0.2}$
XRD	LCCO (200) CaO, CoO, Co_2O_3	CaO, CoO, Co_2O_3
AFM (RMS values)	9 Å	243 Å

Table 2 Optical emission lines selected for the optical spectroscopy studies

Species	Emission wavelength
La(I)	576.1 nm
La(II)	394.9 nm
Ca(I)	585.7 nm
Ca(II)	396.7 nm
Co (I)	393.6 nm
O(I)	777.6 nm

Plume emission in ns and fs ablation has been investigated by time-resolved emission spectroscopy in order to find possible origins of the Co deficiency observed in the films grown by fs ablation. The optical emission spectrum of $La_{0.6}Ca_{0.4}CoO_3$ exhibits many peaks that can be assigned to various atoms and ions. Transitions of neutral Ca (Ca(I)), Co (Co(I)), La (La(I)) and O (O(I)) as well as singly ionized Ca (Ca(II)) and La (La(II)), were identified using the NIST Atomic Spectra Database [20] and are summarized in Table 2. In the case of Co and O species, only Co(I) and O(I) lines were sufficiently intense to be analysed by optical emission spectroscopy.

In the early stages of the plume expansion, a continuum Bremsstrahlung radiation, superimposed on the individual emission lines, is observed at the target surface. Upon cooling of the plume, the continuum decays rapidly and the individual emission lines dominate the spectra. The emission spectra generated by ns and fs ablation in 60 Pa O_2 are shown in Figs. 3a and b, respectively. As seen in Fig. 3a, at early times the emission spectrum generated by ns ablation consists of intense lines assigned to La and Ca ions and weaker ones coming from the corresponding neutral species. After a few hundred nanoseconds, the ionic lines decay while the neutral atom lines, La(I) and Ca(I), increase in intensity due to recombination of the ions with electrons. Similarly, the emission spectrum generated by fs ablation (Fig. 3b) exhibits many atomic and ionic lines. In addition, at times greater than 500 ns, the broad emission bands from CaO are observed in the range of 540–600 nm. The data indicate that during ns ablation of LCCO the ablated material is effectively atomized and that the amount of diatomic species, originating from reactive collisions between ablated atoms and oxygen, is too low to be detected. The presence of intense broadband emission due to diatomic molecules in the plume generated in fs ablation, suggests that the mechanisms of fs ablation, in the plume of LCCO, are different than that of ns ablation.

One of the key parameters determining the quality and composition of the grown films is the kinetic energy of the species of the plume arriving at the substrate. The velocities of the plume species were extracted from time-resolved optical emission spectroscopy data and are listed in Table 3.

Our observations can be summarized as follows.

(i) For ns ablation in vacuum the fastest species are the ions, followed by neutrals, e.g. from Ca(II) to Ca(I) and from La(II) to La(I). The difference in velocities between ions and neutrals has been previously reported in the literature [21] and has been explained by the ambipolar diffusion mechanism [22]. This mechanism suggests that in early times of the plume expansion, the lighter particles (electrons) will diffuse much faster than the heavier particles (ions and neutrals), leading to the formation of an electron rich and electron depleted layer in the plume. This creates an electric field that accelerates the ions and decelerates the electrons, resulting in the observed higher velocity of the Ca(II) compared to Ca(I) species. It is noteworthy that the Ca(I) species are faster than the Co(I) species.

(ii) For fs ablation in vacuum the singly charged species exhibit as well larger velocities than the neutral ones. However, the Co(I) species exhibit a larger velocity than the Ca(I) species, but they are slightly slower than the Ca(II) ones. A direct comparison of the velocities between ns and fs ablation is not possible, since different fluences have been applied in the two cases.

(iii) The velocities of the excited species in the presence of 60 Pa O_2 are lower than in vacuum, due to collisions of the plume with the background gas molecules. In the case of ns ablation, the ionic species are still faster that the neutral ones, while for fs ablation the Ca(II) and La(II) species are slower than the neutral ones. In addition, the Ca(I) species are faster than the Co(I) ones. This suggests that ns ablation in the presence of a background gas is closer to the predicted behavior compared to fs ablation.

3.3 Time-resolved plume imaging for ns and fs ablation

3.3.1 Plume-imaging in vacuum

Time-gated imaging studies allow estimation of the velocity distributions of the various emitting species within the plume [23], and can give additional information about the plume shape and dynamics at different positions from the target. In this study, the plume was imaged along the expansion direction and over a distance of 3 cm from the target surface. The setup used for these experiments did not allow imaging of the plume-substrate interaction, which would correspond to a target to substrate distance of 4 cm. The results of fast imaging of the Co(I) emission induced by ns and fs ablation are shown in Figs. 4a, c, with the corresponding delay times indicated in each image. The images were filtered using a narrow band width filter with a maximum peak at 355 nm and with a FWHM of 10 nm. During ns ablation the plume emission appears to be spherical (Fig. 4a),

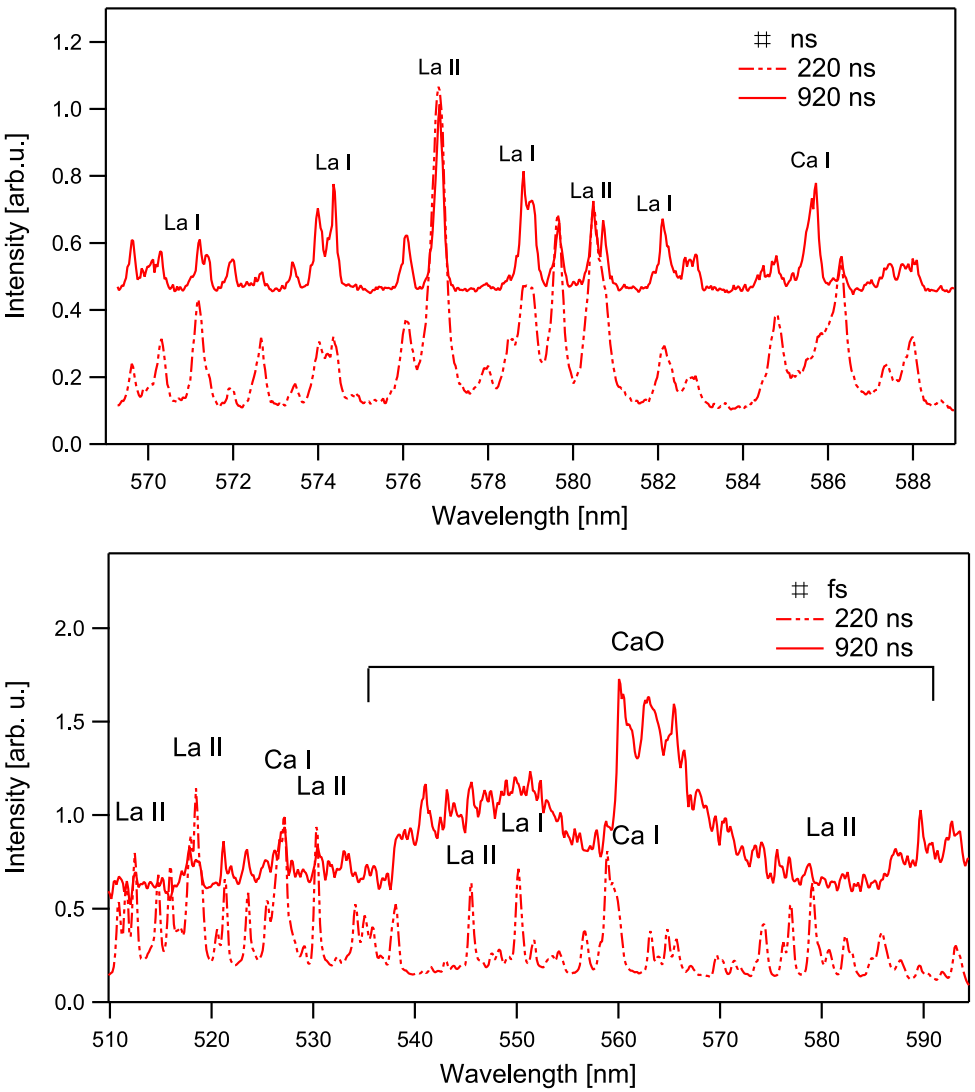

Fig. 3 Optical emission spectra of the plume induced by ns and fs laser ablation of $La_{0.4}Ca_{0.6}CoO_3$ in a pressure of 60 Pa O_2. The spectra correspond to plume emission collected at the target surface ($z = 0$ mm)

while in the case of fs ablation (Fig. 4c) the plume front expands more rapidly into the vacuum, resulting in an elongated shape of the plume. Similar observations have been reported by Santagata et al. [24] for fs laser ablation of AlN. A simple model for the quantitative estimation of the angular distribution of the plume in fs ablation has been suggested which considers the intensity I_0 at the detection angle $\theta = 0$, while the intensity, I_θ , at a greater angle is defined by the relation $I_\theta = I_0 \cos^n(\theta)$, where n is the fitting parameter which defines the plume anisotropy. This model assumes that the shape of the line profiles reflects the spatial distribution of the ejected material. The n parameter is a measure of the orthogonal diameter of each contour plot and in our experiments it was calculated from the plume-imaging profiles at 420 μs. An ideal spherical shape corresponds to $n = 1$. A value of $n = 0.9 \pm 0.2$ was obtained for ns ablation and $n = 1.8 \pm 0.2$ for fs ablation. The data quantify the visual appearance of the elongated plume shape observed in fs ablation.

A similar behavior was observed for the other plume species. The plume emission of the La(II)&Ca(II) in vacuum for ns and fs ablation is depicted in Figs. 4b, d. The images were filtered using a narrow band width filter with a maximum peak at 396.5 nm and with a FWHM of 3.17 nm. Again, the fs pulses induce a more elongated plume along the expansion direction, compared to the ns pulses. At a given time (920 μs) the plume induced by fs ablation appears to have traveled a longer distance compared to the plume induced by ns ablation. The plume front velocities data obtained from the imaging data are summarized in Table 4. The plume front position was defined as the position where the emission intensity decays to 20% of its maximum value. Table 4 indicates higher velocities for the fs ablated species compared to the ns species, with the exception of La(II)&Co(I). A clear order of ions being faster than neutrals is also obtained by plume image analysis for La(II)&Ca(II), while La(II)&Co(I) are slower than the neutral species. This may be due to the fact that ions mixed with neutrals are an-

Table 3 Velocities of the ionic, neutral species (m/s) obtained from emission spectroscopy

	ns		fs	
	Vacuum (m/s)	60 Pa O_2 (m/s)	Vacuum (m/s)	60 Pa O_2 (m/s)
Ca(I)	$1.8(\pm0.1) \times 10^4$	$1.35(\pm0.1) \times 10^4$	$9.2(\pm0.1) \times 10^3$	$1.1(\pm0.1) \times 10^4$
Ca(II)	$1.9(\pm0.1) \times 10^4$	$1.8(\pm0.1) \times 10^4$	$1.5(\pm0.1) \times 10^4$	$7.2(\pm0.1) \times 10^3$
La(I)	–	$1.4(\pm0.1) \times 10^4$	$1.3(\pm0.1) \times 10^4$	$1.2(\pm0.1) \times 10^4$
La(II)	$1.8(\pm0.1) \times 10^4$	$1.7(\pm0.1) \times 10^4$	$1.9(\pm0.1) \times 10^4$	$9.1(\pm0.1) \times 10^3$
Co(I)	$1.4(\pm0.1) \times 10^4$	–	$1.3(\pm0.1) \times 10^4$	$7.7(\pm0.1) \times 10^3$

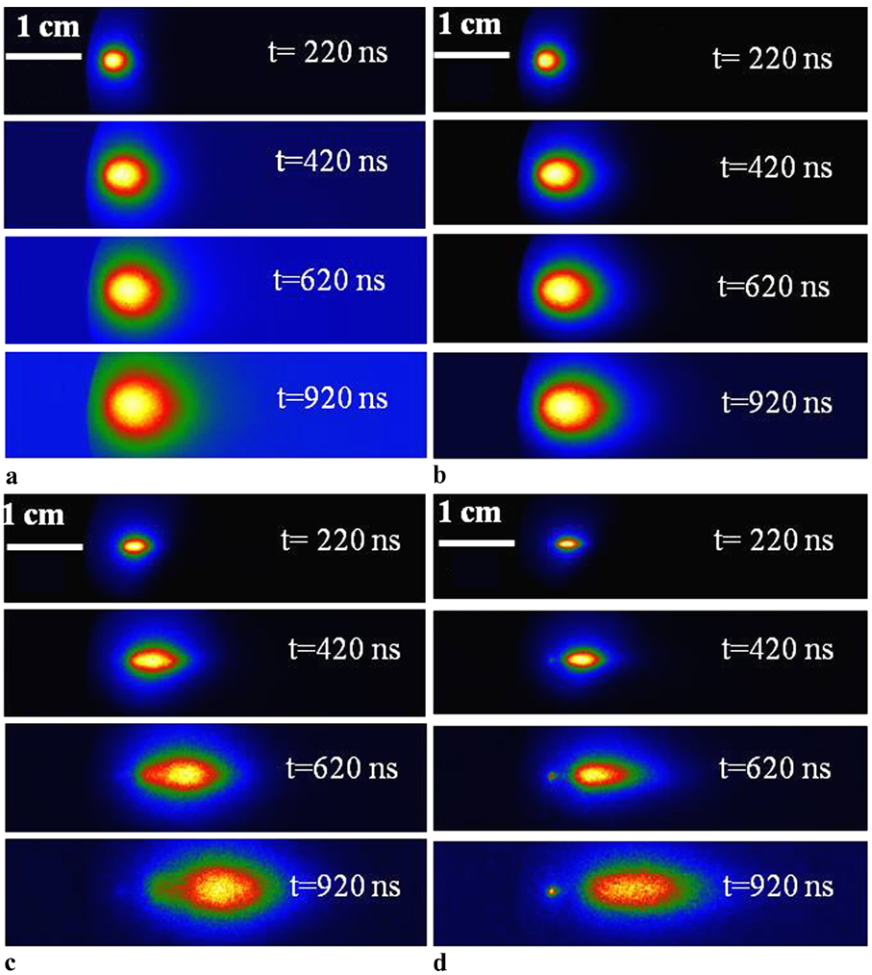

Fig. 4 Wavelength filtered ICCD images of the Co(I) species for ns ablation (**a**) and fs ablation (**c**), and of the La(II)&Ca(II) species for ns ablation (**b**) and fs ablation (**d**). The images were taken in vacuum

alyzed with various intensities for the different species. The highest plume front velocity is observed for Co(I) in ns ablation while in fs ablation the Co(I) species and the La(II) &Ca(II) are the fastest.

Furthermore, the ICCD plume images allow the extraction of information about the plume velocity distribution. The profiles corresponding to the Co(I) species for fs ablation in vacuum are shown in Fig. 5. The images were taken at different delay times, 120 ns, 320 ns, 520 ns, 720 ns, and 920 ns. At early times, $t < 320$ ns, the plume emission profile for Co(I) exhibits a single mode distribution. After $t = 520$ ns, the emission becomes broader and two peaks become visible. The first peak, located at ~4 mm from the target surface, travels at a velocity similar to other species in the plume. The second distribution, not observed for the other species in the plume, has a maximum at a distance of 10 mm. The maximum intensity of Co(I), I_M, plotted as a function of distance from the target is shown in Fig. 6. Up to a distance of 4 mm, I_M of Co(I) reveals a similar decay to La(II)& Ca(II), while at larger distances a slower decrease of intensity is observed. The plot indicates the presence of a long lasting population up to 14 mm from the target sur-

Table 4 Plume front velocities (m/s) obtained from the plume-imaging data. Note that pairs of species, La(II)&Ca(II) and La(II)&Co(I), were imaged when the optical filter could not distinguish between individual emission lines

Species	Nanosecond ablation			Femtosecond ablation		
	Vacuum	60 Pa O_2 (*)	SKW	Vacuum	60 Pa O_2 (*)	SKW
La(II)&Ca(II)	1.6×10^4	1.6×10^4	$a \times t^{2/5}$	2.5×10^4	2.4×10^4	$a \times t^{0.4}$
La(II)&Co(I)	1.9×10^4	1.9×10^4	$a \times t^{2/5}$	8.0×10^3	9.2×10^3	$a \times t^{0.3}$
Co(I)	2.1×10^4	1.8×10^4	$a \times t^{2/5}$	2.4×10^4	8.8×10^3	$a \times t^{0.36}$
Ca(I)	1.4×10^4	2.0×10^4	$a \times t^{2/5}$	2.0×10^4	7.0×10^3	$a \times t^{0.45}$

(*)(velocities extracted from the free-flight region)

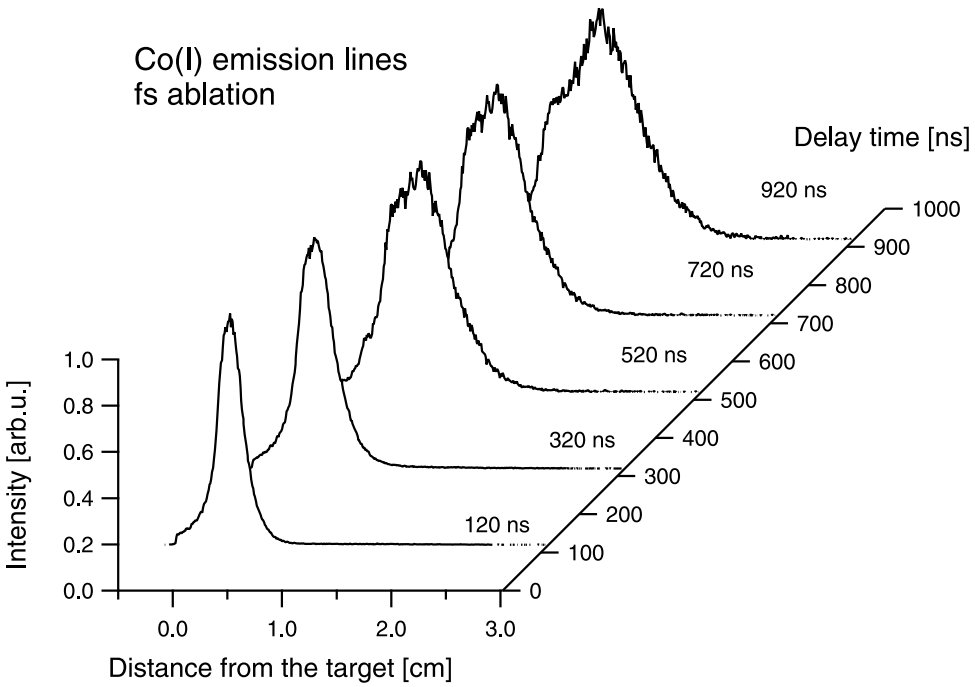

Fig. 5 Plume emission intensity profiles for the Co(I) species in fs ablation in vacuum. The plots correspond to images collected at a delay time of 120 ns, 320 ns, 520 ns, 720 ns and 920 ns

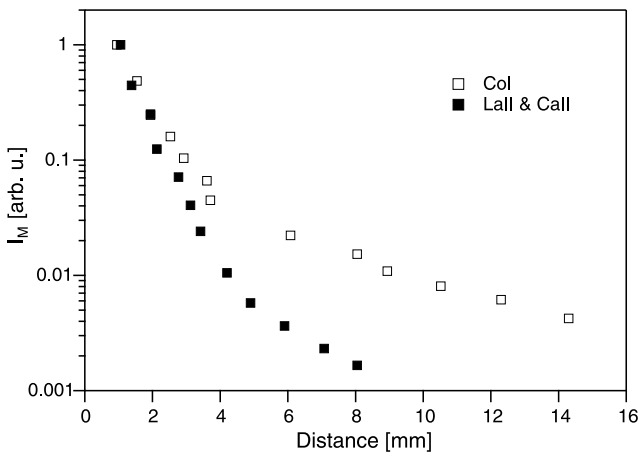

Fig. 6 Fs ablation: maximum emission intensity, I_M, versus distance from the target surface for Co(I) and La(II)&Ca(II) species

face which is attributed to the second population of the Co(I) species in the plume.

3.3.2 *Plume expansion in an oxygen background pressure of 60 Pa*

Similar experiments were performed in the presence of 60 Pa O_2 background gas, which are the typical conditions for films deposition in ns ablation and where poor crystallinity and strong deviation in the Co content for films grown by fs ablation were observed. The emission of the Co(I) species for ns and fs ablation are shown in Figs. 7a and c, respectively, while Figs. 7b and d show the emission of La(II) &Ca(II) species for ns and fs ablation, respectively. During expansion in a background gas, the plume undergoes multiple scattering with the oxygen molecules, resulting in a spatial splitting into species which travel without collisions (fast) and species undergoing collisions (slow). This effect has been reported in the literature [21], and is observed for

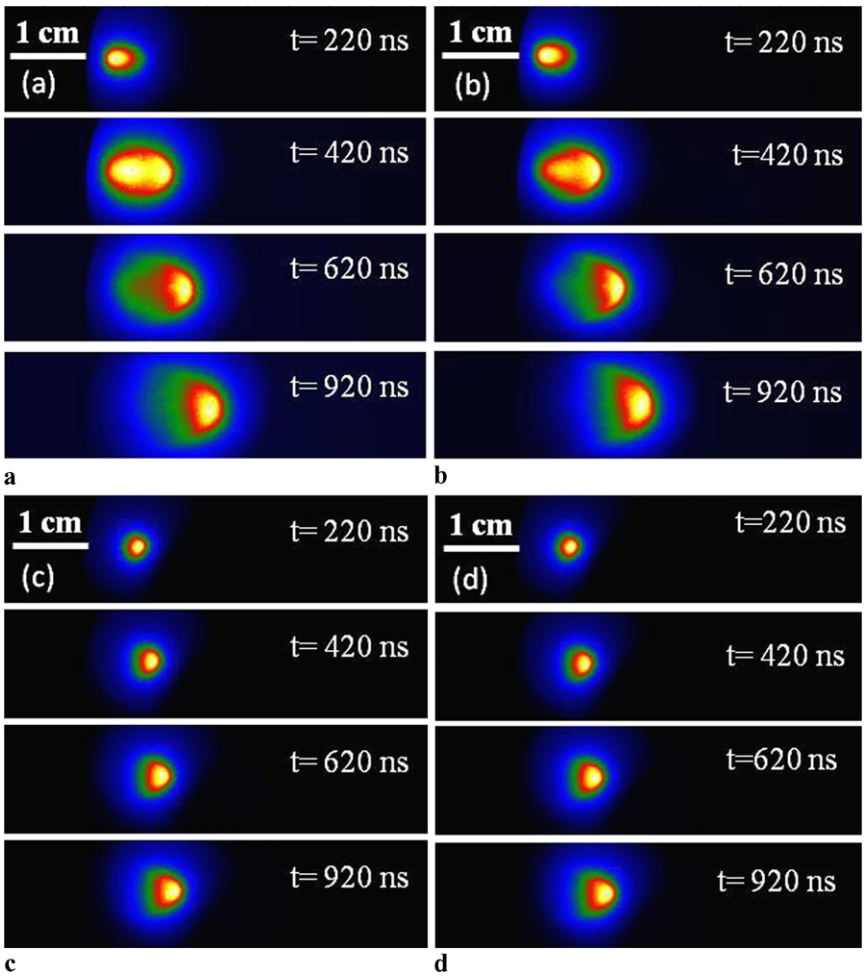

Fig. 7 Wavelength filtered ICCD images of the Co(I) species for ns ablation (**a**) and fs ablation (**c**), and of the La(II)&Ca(II) species for ns ablation (**b**) and fs ablation (**d**). The images were taken in presence of 60 Pa O_2

both ions and neutrals. The velocities of the plume front extracted from the free-flight region of the plume are given in Table 4. In ns ablation the plume front position follows a $\tau^{2/5}$ time dependence, in agreement with the shock wave (SKW) propagation model in gases [25]. In the case of fs ablation, a $\tau^{0.3-0.45}$ dependence is obtained, indicating that the plume front does not follow the behavior predicted by the shock wave model (see Table 4). We can therefore conclude that the SKW model cannot be used to fit the fs plume expansion at a background pressure of 60 Pa O_2, which again indicates the different mechanism of fs ablation.

4 Discussion

Our data show that it is difficult to grow high-quality films of $La_{0.6}Ca_{0.4}CoO_3$ by fs laser ablation. The $La_{0.6}Ca_{0.4}CoO_3$ films grown by fs ablation do not present a perovskite crystalline structure and do not have the same composition as the target, i.e. Co deficiency is observed. At the same time, we have shown that well oriented films of $La_{0.6}Ca_{0.4}CoO_3$ with a low amount of additional phases can be obtained by ns-PLD.

Previous literature reports have shown that simple oxide films, such as ZnO grown by fs-PLD present a poorer crystallinity than those obtained by ns-PLD [26, 27]. These differences have been assigned to the high kinetic energy of the species generated in fs regime compared to those emitted in the ns regime. However, Brodoceanu et al. [28] have shown that polycrystalline $La_{0.5}Sr_{0.5}CoO_3$ films can be deposited at low fluence by fs-PLD (50 fs pulse duration, 800 nm wavelength).

First we would like to discuss the simpler case of the ablation in vacuum, which can be used as reference for later studies in the oxygen background.

The plume front velocities in vacuum are slightly higher in fs ablation compared to ns ablation, despite the fact that a lower fluence was used for fs ablation (3 J cm^{-2} versus 5 J cm^{-2}). The highest velocities in fs ablation were found for Co(I) and La(II)&Ca(II) species. The small differences in the velocities of the species in fs ablation compared to ns ablation could not explain the deviations of the Co content in the growing films. Plume-imaging data, shown in Fig. 5a, indicate that the spatial profile of the Co(I) along the expansion direction consists of at least two species. The first one is observed near the target surface, while the second domi-

nates at distances larger than 4 mm. The first distribution is similar to the other plume species and it can be assigned to neutral Co(I) generated during ablation.

The presence of two groups of species during laser ablation of Cr_2O_3 in vacuum has also been reported by Dinescu et al. [29]. One group has been assigned to originate from direct ablation, while the second one is created by the neutralization of ions along the plume path. However, if, in our case, the electron- ion recombination processes in the plume ($Co(II) + e^- \rightarrow Co(I)$) are responsible for the existence of the second species with higher velocity, then the Co(II) species must be initially faster than the other ions in the plume (or the same behavior would be observed for all species), which is not the case (see Table 4). This suggests that the second distribution of Co(I) species in the plume is not likely to result from neutralization of single ions. One possible source leading to the presence of the second population of Co(I) in the plume may originate from the dissociation of cobalt oxide species or larger clusters during expansion in vacuum. Gonzalo et al. [30] reported also a double population of Bi(I) species during fs laser ablation of $Bi_{12}GeO_{20}$. The second population of Bi has been assigned to the dissociation of oxide clusters/molecules species during the plasma expansion either by direct dissociation or via electron impact processes. Cluster formation in fs ablation has been previously reported and may result from a Coulomb explosion or phase explosion [31]. The presence of oxides clusters of CoO_x cannot be detected by optical emission spectroscopy, but ejection of clusters has been often detected by mass spectrometry [31]. Imaging of the plume-substrate interaction [32] may be of a great importance for future studies.

Studies of the plumes generated by fs and ns ablation in vacuum indicate that there are differences in the ablation and plume generation mechanisms.

In the presence of a background pressure of 60 Pa O_2 only minor differences in the plasma plume are observed. The ns ablated species are attenuated in time according to the shock wave model, i.e. with a $\tau^{2/5}$ time dependence, while for fs laser ablation, where Co depletion in the growing films was observed, the plume front attenuation does not follow the predicted time dependence estimated by the SKW model. The plume shape and velocity of species in the O_2 background is also similar for ns and fs ablation, most probably due to collisions with oxygen which slow down the fast species (see Fig. 7c, d). A non-uniform distribution of elements in the plasma, as reported for Ba in $BaTiO_3$ [33] and Li in $LiMn_2O_4$ [21] is also not likely because no pronounced differences in the distribution of the elements is detected. The small differences in the kinetic energies of the ablated species are probably not being enough to explain the non stoichiometric transfer in fs ablation. The reasons for Co deficiencies in the case of fs irradiation in the growing films with O_2 background gas are therefore not clear.

Possible mechanisms for losses of cobalt in fs-PLD may be related to the following:

(i) Different angular distributions of the species in the plume, which was not observed;
(ii) If we assume that the sticking coefficient is the same for all elements, the observed changes in the composition of the films may be related to the presence of Co clusters in the fs-induced plasma, as previously reported for fs ablation of other oxides [34]. Co-rich clusters may partially dissociate during plume expansion or arrive at the substrate as Co-rich clusters and not participate to the film growth. The decrease in the sticking coefficient of the Co clusters could explain the Co deficiency observed in fs ablation. The reasons why the formation of Co-rich clusters would be favorable and why clusters would have a lower sticking probability is not clear.

5 Conclusion

In this work, we have shown that large differences in the crystalline properties and stoichiometry of $La_{0.6}Ca_{0.4}CoO_3$ films grown by nanosecond or femtosecond PLD exist. Laser ablation of $La_{0.6}Ca_{0.4}CoO_3$ using ultrashort pulses, i.e. 500 fs at 248 nm, results in pronounced Co deficiencies, which are not present for ns ablation, i.e. 20 ns at 248 nm applying similar fluences. The plume shape in vacuum is spherical for ns ablation, while for fs ablation the plume shape is elliptical, but plume front velocities are rather similar. Plume-imaging studies reveal the presence of two species of Co(I) in fs ablation under vacuum, different from ns ablation where only one single distribution of Co(I) species is observed. The ejection of cluster oxides during fs ablation, followed by their partial dissociation during expansion may contribute to the double distribution of Co(I).

With a background pressure of O_2, no pronounced differences between the velocities of the plume species, the plume shapes, and distribution of the plume species for fs and ns ablation are observed. The possible mechanisms for the depletion of certain atomic species in the films which have been reported for ns and fs laser ablation previously, i.e. different angular distributions of the species in the plume and/or high kinetic energy plasma species, are not likely to be the origin for the Co depletion in LCCO films deposited by fs ablation. One possible mechanism could be the emission of Co or Co-rich clusters during fs ablation which do not participate in the films growth. The reason why these clusters should not stay on the substrate and why only Co-rich clusters should be formed is not clear.

Acknowledgements Financial support from the Swiss National Science Foundation is gratefully acknowledged. SC and MJM acknowledge support from the EC through LaserLab Europe (FP6-RII3-CT-2003-506350) and a Marie Curie fellowship (FP5-HPMT-GH-00-00177-15), respectively, which allowed them to perform experiments at ULF-FORTH, Greece.

References

1. A. Ovsianikov, B.N. Chichkov, *Nanoelectronics and Photonics* (Springer, New York, 2008)
2. K. Sasaki, S. Inoue, K. Nishio, H. Masuda, A. Otomo, S. Yokoyama, Opt. Mater. **32**, 543 (2010)
3. H.Y. Zheng, Z.W. Jiang, J. Micromech. Microeng. **20**, 017001 (2010)
4. K. Hatanaka, T. Ida, H. Ono, S. Matsushima, H. Fukumura, S. Juodkazis, H. Misawa, Opt. Express **17**, 12650 (2008)
5. R. Wagner, S.Y. Chen, A. Maksimchuk, D. Umstadter, Phys. Rev. Lett. **78**, 3125 (1997)
6. C.L. Gordon, J.J. Macklin, B.E. Lemoff, G.S. Brown, S.E. Harris, Phys. Rev. Lett. **68**, 1527 (1992)
7. E.L. Clark, K. Krushelnick, M. Zepf, F.N. Beg, M. Tatarakis, A. Machacek, M.I.K. Santala, I. Watts, P.A. Norreys, A.E. Dangor, Phys. Rev. Lett. **85**, 1654 (2000)
8. G. Pretzler, A. Saemann, A. Pukhov, D. Rudolph, T. Schätz, U. Schramm, P. Thirolf, D. Habs, K. Eidmann, G.D. Tsakiris, J. Meyer-ter-Vehn, K.J. Witte, Phys. Rev. E **58**, 1165 (1998)
9. G.A. Mourou, C. R. Acad. Sci., Sér. IV Phys. Astrophys. **10**, 1407 (2001)
10. K.J. Gaffney, H.N. Chapman, Science **5830**, 1444 (2007)
11. E. Rebollar, S. Gaspard, M. Oujja, M.M. Villavieja, T. Corrales, P. Bosch, S. Georgiou, M. Castillejo, Appl. Phys. A, Mater. Sci. Process. **84**, 171 (2006)
12. J. Budai, M. Bereznai, G. Szakács, E. Szilágyi, Z. Tóth, Appl. Surf. Sci. **253**, 8235 (2007)
13. C. Ghica, C. Ristoscu, G. Socol, D. Brodoceanu, L.C. Nistor, I.N. Mihailescu, A. Klini, C. Fotakis, Appl. Surf. Sci. **252**, 4672 (2006)
14. A. Hu, M. Rybachuk, Q. Lu, W.W. Duley, Diam. Relat. Mater. **17**, 1643 (2008)
15. M. Stock, P. Molian, J. Vac. Sci. Technol., A, Vac. Surf. Films **22**, 670 (2004)
16. T. Csákó, J. Budai, T. Szörényi, Appl. Surf. Sci. **252**, 4707 (2006)
17. M.J. Montenegro, M. Döbeli, T. Lippert, S. Muller, B. Schnyder, A. Weidenkaff, P.R. Willmott, A. Wokaun, Phys. Chem. Chem. Phys. **4**, 2799 (2002)
18. S. Müller, O. Haas, C. Schlatter, C. Comninellis, J. Appl. Electrochem. **28**, 305 (1998)
19. M. Montenegro, PhD thesis, Zürich, 2004
20. NIST bibliographic database
21. S. Canulescu, E.L. Papadopoulou, D. Anglos, T. Lippert, C.W. Schneider, A. Wokaun, J. Appl. Phys. **105**, 063107 (2009)
22. M. Tanaka, Y. Fujisawa, T. Nakajima, Y. Tasaka, K. Ota, S. Usami, J. Appl. Phys. **83**, 3379 (1998)
23. F. Claeyssens, M.N.R. Ashfold, E. Sofoulakis, C.G. Ristoscu, D. Anglos, C. Fotakis, J. Appl. Phys. **91**, 6162 (2002)
24. A. Santagata, V. Marotta, S. Orlando, R. Teghil, M. Zaccagnino, A. Giardini, Appl. Surf. Sci. **208**, 101 (2003)
25. S. Amoruso, A. Sambri, X. Wang, Appl. Surf. Sci. **253**, 7696 (2007)
26. J. Perrière, E. Millon, W. Seiler, C. Boulmer-Leborgne, V. Craciun, O. Albert, J.C. Loulergue, J. Etchepare, J. Appl. Phys. **91**, 690 (2002)
27. A. Klini, A. Manousaki, D. Anglos, C. Fotakis, J. Appl. Phys. **98**, 123301 (2005)
28. D. Brodoceanu, A. Manousaki, I. Zergioti, A. Klini, M. Dinescu, C. Fotakis, Appl. Phys. A, Mater. Sci. Process. **79**, 911 (2004)
29. G. Dinescu, M.N. Oliveira, O. Conde, Appl. Surf. Sci. **208-209**, 90 (2003)
30. J. Gonzalo, J.M. Ballesteros, C.N. Afonso, Appl. Surf. Sci. **138**, 52 (1999)
31. A.V. Bulgakov, I. Ozerov, W. Marine, Appl. Phys. A, Mater. Sci. Process. **79**, 1594 (2004)
32. S. Amoruso, C. Aruta, R. Bruzzese, X. Wang, U.S. di Uccio, Appl. Phys. Lett. **98**, 101501 (2011)
33. E. Millon, J. Perrière, R.M. Défourneau, D. Défourneau, O. Albert, J. Etchepare, Appl. Phys. A, Mater. Sci. Process. **77**, 73 (2003)
34. M. Sanz, M. Castillejo, S. Amoruso, G. Ausanio, R. Bruzzese, X. Wang, Appl. Phys. A, Mater. Sci. Process. **101**, 639 (2010)